

Article

Effect of Polishing-Induced Subsurface Impurity Defects on Laser Damage Resistance of Fused Silica Optics and Their Removal with HF Acid Etching

Jian Cheng ^{1,*}, Jinghe Wang ¹, Jing Hou ², Hongxiang Wang ¹ and Lei Zhang ¹

¹ School of Mechatronics Engineering, Harbin Institute of Technology, Harbin 150001, China; hitwjh@163.com (J.W.); whx@hit.edu.cn (H.W.); emailzhanglei@126.com (L.Z.)

² Research Center of Laser Fusion, China Academy of Engineering Physics, Mianyang 621900, China; houjing1997@163.com

* Correspondence: cheng.826@hit.edu.cn; Tel.: +86-451-8640-3252

Academic Editor: Federico Pirzio

Received: 11 July 2017; Accepted: 11 August 2017; Published: 15 August 2017

Abstract: Laser-induced damage on fused silica optics remains a major issue that limits the promotion of energy output of large laser systems. Subsurface impurity defects inevitably introduced in the practical polishing process incur strong thermal absorption for incident lasers, seriously lowering the laser-induced damage threshold (LIDT). Here, we simulate the temperature and thermal stress distributions involved in the laser irradiation process to investigate the effect of impurity defects on laser damage resistance. Then, HF-based etchants (HF:NH₄F) are applied to remove the subsurface impurity defects and the surface quality, impurity contents and laser damage resistance of etched silica surfaces are tested. The results indicate that the presence of impurity defects could induce a dramatic rise of local temperature and thermal stress. The maximum temperature and stress can reach up to 7073 K and 8739 MPa, respectively, far higher than the melting point and compressive strength of fused silica, resulting in serious laser damage. The effect of impurity defects on laser damage resistance is dependent on the species, size and spatial location of the defects, and CeO₂ defects play a dominant role in lowering the LIDT, followed by Fe and Al defects. CeO₂ defects with radius of 0.3 μm, which reside 0.15 μm beneath the surface, are the most dangerous defects for incurring laser damage. By HF acid etching, the negative effect of impurity defects on laser damage resistance could be effectively mitigated. It is validated that with HF acid etching, the number of dangerous CeO₂ defects is decreased by more than half, and the LIDT could be improved to 27.1 J/cm².

Keywords: fused silica; ultra-precision polishing; subsurface damage; laser damage resistance; absorbing impurity defects; HF acid etching

1. Introduction

In order to achieve clean and sustainable energy resources, high-power laser systems have been developed worldwide for pursuing inertial confinement fusion (ICF), such as the National Ignition Facility (NIF) in the United States [1,2], the Laser MegaJoule (LMJ) in France [3], the High Power laser Energy Research facility (HiPER) in Europe [4] and the ShenGuang (SG)-III laser facility in China [5]. To obtain the extremely high pressure and temperature required for ICF ignition, a huge amount of large-aperture optics with high precision surfaces are required to temporally, spatially and spectrally control the laser beams. The laser beams are finally coupled together, focusing simultaneously on a very tiny target filled with fusion fuels. Among these optics, fused silica is an amorphous state of silicon dioxide, which has extremely low thermal conductivity, super strong thermal-shock resistance, low dielectric loss, and high deformation (1370 K) and softening (2000 K) temperatures. Besides, the

fused silica optics possess such broad optical transmission spectra that over 1000 pieces of silica optics have been widely used in the sub-laser systems with fundamental (1ω) and triple (3ω) frequencies of the ICF facilities. The fused silica optics serve as switch and vacuum windows, wedged focus lens, diffraction grating, debris shields and so on [6,7]. Since the fused silica optics are exposed to high-power lasers in their actual applications, the well prepared engineering silica components should have very high laser damage resistance. However, due to the weak mechanical properties of fused silica, the introduction of undesirable by-products (viewed as defects) on the surface or subsurface of finished brittle silica parts in the actual cutting, grinding, polishing, coating and cleaning processes is inevitable. The surface and subsurface defects can extend downward several to tens of microns beneath the finished surface, which would greatly lower the energy output capacity of the ICF laser facilities. Currently, thanks to the development of various new advanced processing techniques (e.g., laser conditioning [8], thermal annealing [9,10]), the bulk laser-induced damage threshold (LIDT) of fused silica can reach up to $475 \pm 25 \text{ GW/cm}^2$ (1064 nm, 8 ns), which is very close to the theoretically intrinsic LIDT and almost one order of magnitude higher than the surface LIDT [11]. This means that the laser-induced damage on surface and subsurface of fused silica plays a dominant role in restricting the promotion of energy output capacity of ICF facilities. Similar to the fused silica optics applied in high power laser systems, many other optical materials (e.g., potassium dihydrogen phosphate KDP as well as its deuterated analog DKDP, fluoride and selenide crystals) are also expected to possess high optical qualities, like optical transparency and laser damage threshold [12–15]. For these crystal materials, rapid growth of large-size boules with desired optical properties has been being a great challenge, and the growth conditions are susceptible to affect the crystal structures, which is closely associated with the bulk laser damage threshold. As a result, the efforts to promote the optical properties of these optical materials are mainly focused on exploring the mechanisms of bulk laser-induced damage and optimizing the growth parameters to improve the crystal structures for increasing the bulk LIDT [14–16]. For fused silica optics, though the internal structure of silica is stable and robust, its hard and brittle characteristics would make the ultra-precision manufacturing of defect-free silica surfaces a great challenge. Therefore, the study on laser damage of fused silica optics should primarily aim at the defects on a finished surface or subsurface. It is of great theoretical and practical significance to explore the underlying mechanisms involved in the laser-induced surface damage and develop new engineering techniques to remove the surface and subsurface defects for improving the laser damage resistance of fused silica.

The primary source leading to the low surface LIDT of fused optics is the subsurface damage (SSD) caused in the chemical-mechanical polishing process. The SSD layer located beneath the polished surface generally consists of re-deposition layer (also named the Beilby layer), a defect layer with crack and scratch defects included, and a deformed layer [17–19]. During the polishing process, the highly absorptive impurities (e.g., Ce, Fe, etc.) coming from the polishing slurries are randomly distributed among the re-deposition layer. Some of the impurities are even embedded and hidden deeply inside the defect layer via entering the open subsurface cracks and scratches. Under the irradiation of intense laser, the impurity defects would make the natively transparent fused silica optics highly absorptive to incident laser, resulting in very high local temperature and stress, and eventually the breakdown of the optical parts [7,20,21]. Meanwhile, the absorptive impurity defects would change the initial band-gap structure of fused silica and also trigger new photon excitation under intense laser irradiation. These effects caused by the impurity defects would substantially affect the laser-induced nonlinear excitation of dielectric silica optics (e.g., multi-photon and avalanche ionizations), making the optical material more susceptible to laser damage [22,23]. The absorptive impurities mainly originate from three kinds of sources in the optical processing stage: oxide polishing slurries (CeO_2 , ZrO_2 , etc.), metal polishing tools (Fe, Cu, Cr, etc.) and Al ion from optical cleaning. Hu et al. [24] demonstrated that besides subsurface scratch and dig defects, ~35% of the laser damage sites were initiated at invisible defects, probably being absorptive impurities with submicrometer size. It was also experimentally proved by Neauport et al. [17,25] that the laser-induced damage on fused silica was closely associated with the

subsurface absorptive impurities and different types of impurity defects would incur different levels of optical damage. Hence, in this work, the heat conduction and thermo-elastic equations involved in the absorbing process of impurity defects under intense laser irradiation are firstly numerically resolved using the finite element method (FEM). Then, the temperature and thermal stress distributions inside fused silica caused by impurity defects are investigated to figure out the most dangerous species and size range of impurity defects in decreasing the laser damage resistance of silica optics. This part of work could provide further understanding of the laser-induced damage mechanisms on optical components, which are beneficial to the surface/subsurface quality evaluation and SSD removal of ultra-precision fabricated fused silica optics.

To alleviate the effect of SSD defects on the laser damage resistance of fused silica optics, many engineering techniques (e.g., hydrofluoric HF acid etching [26–28], ultraviolet or CO₂ laser preprocessing [8,29], plasma etching [30], and magneto-rheological finishing (MRF) [31], etc.) have been developed and applied in the actual preparation processes of high-quality silica surfaces. In the laser preprocessing process, lasers with energy lower than the LIDT are used to irradiate the fused silica surfaces. Due to the strong absorption of silica material to CO₂ lasers, the temperature on the optical surface would moderately rise, resulting in the recombination of surface micro-structure and the healing of subsurface cracks. At the same time, the lasers can bring about the electronic excitation of the impurity defects, which would finally lower the defect energy band to a steady state. Hence, this processing technique is able to mitigate the negative effect of impurity defects and subsurface cracks on the laser damage resistance of fused silica. However, there are some shortcomings that need to be urgently solved as well. For example, the temperature gradient in laser heated zone can produce high residual thermal stress and the surface figure error caused by laser preprocessing may induce wavefront distortion, which greatly limits the capacity and advancement of this technique in improving the laser damage resistance [32]. For the plasma etching process, carbon tetrafluoride (CF₄) gas is necessary for effectively etching the silica materials. However, the CF₄ gas and its residual etching reaction product may become new sources of impurity defects, polluting the processed surface and consequently influencing the effect of improving the laser damage resistance [30]. However, high-quality optical surfaces with low roughness and few SSD defects can be achieved with the MRF method, and the magnetic Fe-ion defects from the magnetorheological fluid may be deposited inside the finished optical surfaces, resulting in low LIDT. However, for the HF acid etching technique, polished fused silica optics are immersed in various HF-based etchants (HF or NH₄F:HF mixed solutions with various ratios) to remove the re-deposition layer and partial SSD defects. With the HF acid etching, the crack and scratch defects hidden in deep subsurface of fused silica can be blunted and no new impurity defects would be introduced as well [26]. Besides, under the assistance of megahertz-frequency agitation, the scouring effect of micro jet on the cleaned optical surfaces could be enhanced, causing the micro-particles and impurity defects adhering to the optical surface/subsurface to be further removed [28,33]. As a result, the laser damage resistance of finished fused silica would be greatly enhanced. In the latter part of this work, the HF acid etching technique is employed to remove the SSD defects on fused silica. Then, the etching rate, impurity contents, surface quality and laser damage resistance of etched silica samples are thoroughly investigated and analyzed to validate the role of the HF acid etching technique in removing the subsurface impurity defects and promoting the laser energy capacity of fused silica.

2. Theory and Methods

2.1. Modeling of Impurity-Induced Temperature and Thermal Distributions

The residual impurity defects are generally distributed inside the SSD layers of ground and polished fused silica optics. The laser energy absorbed by these impurity defects is far greater than that by intrinsic thermal absorption of the fused silica itself. On the one hand, the strong absorption of these impurity defects can locally heat the silica materials, inevitably resulting in unsteady and non-uniform

temperature distribution. When the local temperature reaches a certain degree, the optical material may suffer from modification, softening, melting and even boiling, which would certainly incur laser-induced damage [7]. On the other hand, the great temperature gap inside silica materials caused by the absorption of impurity defects could give rise to internal thermal stress, and correspondingly leads to the negative effects of obvious wavefront distortion and weak mechanical strength. These negative effects would directly affect the laser energy capacity and service life of large-aperture fused silica optics [20,21]. In the present efforts, the heat transfer and thermo-elastic equations governing the laser energy absorbing process are numerically solved by adopting the FEM method to investigate the distributions of temperature and thermal stress induced by impurity defects. The effects of subsurface impurity defects with various species and dimensions on the laser damage resistance are then analyzed, based on which we finally clarify the most dangerous impurity defects in terms of lowering the LIDT of fused silica optics.

When the incident laser falls on the silica surface, most of the laser energy is reflected at the interface or transmitted through the bulk, leaving only a fraction of the laser energy absorbed by the materials [34]. As the absorbed energy penetrates, the temperature on fused silica materials increases. The spatially and temporally increasing temperature can be described by the heat transfer equation in the Cartesian coordinate system which is given below [35]:

$$\frac{\partial T}{\partial \tau} = \alpha \left(\frac{\partial^2 T}{\partial x^2} + \frac{\partial^2 T}{\partial y^2} + \frac{\partial^2 T}{\partial z^2} \right) + \frac{q_v}{\rho c} \quad (1)$$

where, T , α , c and ρ represent the temperature, thermal diffusivity, specific heat capacity, and density, respectively. q_v indicates the heat source determined by the incident laser, which can be expressed as [36]:

$$q_v = \alpha \frac{(1-R)P}{\pi a^2} \exp\left(-\frac{x^2+y^2}{a^2}\right) \exp(-\alpha z) \quad (2)$$

with α the absorption coefficient, R the Fresnel reflection coefficient, P the incident laser power, and a the radius waist at $1/e$.

As the laser irradiates the optical surface, part of the heat energy is transported into the bulk, resulting in the rise of surface temperature. Thermal radiation would take place at the hot surface. Besides, the high temperature on the surface may cool down by exchanging heat energy with the ambient air in the form of thermal convection. Hence, the below boundary conditions of heat flux, natural convection cooling and surface-to-ambient radiation are all applied to fully describe the heat transfer process in fused silica under the intense laser irradiation [37]. Under the control of Equation (3), the energy balance would be actually realized by transferring the energy among the sample surface, sample bulk and the surrounding circumstance during the laser heating and natural cooling processes.

$$I\Delta\tau = -k\frac{\partial T}{\partial z} + h(T_s - T_0) + \sigma\varepsilon(T_s^4 - T_0^4) \quad (3)$$

where, k , h and ε are the heat conductivity, convection coefficient, and radiation coefficient, respectively. T_s and T_0 denote the temperatures of fused silica surface and indoor air temperature. I represents the incident laser intensity and Δt indicates the laser action period. σ is the Boltzmann constant.

The historical temperature evolution on fused silica optics can be obtained by numerically solving the heat transfer equation of Equation (1) with the consideration of boundary conditions of Equation (3). It is worth noting that in this work we only focus on the temperature evolution inside the laser spot for the reason that the amount of heat energy transferred outside the light spot is much smaller.

Under the irradiation of the Gaussian laser pulse, the thermal distortion caused by absorptive impurity defects could be resolved and analyzed on the basis of the temperature distribution obtained

from Equation (1). Ignoring the volume and inertia forces inside fused silica, the thermal distortion arising from internal temperature gradient would be described as follows [38]:

$$\begin{cases} \nabla^2 u_r - \frac{u_r}{r^2} + \frac{1}{1-2\nu} \frac{\partial e}{\partial r} - \frac{2(1+\nu)}{1-2\nu} \alpha_t \frac{\partial T}{\partial r} = 0 \\ \nabla^2 u_z + \frac{1}{1-2\nu} \frac{\partial e}{\partial z} - \frac{2(1+\nu)}{1-2\nu} \alpha_t \frac{\partial T}{\partial z} = 0 \end{cases} \quad (4)$$

where u_r and u_z are the displacement components in r and z directions of cylindrical coordinate system. e represents the volumetric strain of fused silica. ν and α_t are the Poisson’s ratio and coefficient of thermal expansion, respectively. Using the relations between stress and strain, the expression of potential energy principle can be gained based on the principle of virtual work. Then, by dispersing the potential energy expression and solving the nodal displacement matrix with the FEM method, we would obtain the corresponding thermal stress distribution initiated by the absorptive impurity defects.

With the application of advanced testing techniques like synchrotron radiation X-ray fluorescence (SXRF) and secondary ion mass spectrometry (SIMS), it has been previously reported [17,18,20,22,25] that the precision grinding and polishing of optical materials can probably introduce impurity defects with sub-wavelength size on the processed surface or subsurface. The impurity defects mainly contain cerium oxide (CeO_2), zirconium dioxide (ZrO_2), iron (Fe), aluminum (Al), chromium (Cr) and so on [17,20,25]. In this work, we choose CeO_2 , Fe and Al as the three representative defects coming from the oxide polishing slurries, metal polishing tools and cleaning solutions, respectively. The effects of defect species, size and spatial location are all investigated and compared to reveal the most dangerous impurity to laser damage resistance. The optical and thermodynamic parameters of fused silica and impurity defects are exhibited in Tables 1 and 2, respectively. It should be noted that the optical damage of fused silica materials initiated by impurity defects under intense laser irradiations is really a complex process, which involves in the material modification, softening, melting, boiling, material fracture and even ejection. All of these processes are closely associated with the rise of temperature and stress during the energy absorption of incident lasers. Therefore, in the present work, the material definition models for both fused silica and impurity defects are simplified with constant thermodynamic parameters to model the temperature and stress distributions caused by representative impurity defects for evaluating their effects on the laser damage resistance.

Table 1. Thermodynamic parameters of fused silica materials used in calculations [39,40].

| Property | Nomenclature | Value (Units) |
|---------------------------------|--------------|--|
| Molar mass | M | 60.06 (g/mol) |
| Crystal system | – | Amorphous |
| Density | ρ | 2.21 (g/cm ³) |
| Melting point | T_m | 1900 (°C) |
| Thermo-optical coefficient | ϵ | 1×10^{-5} |
| Coefficient of linear expansion | α_t | $5.5 \times 10^{-7} \text{ }^\circ\text{C}^{-1}$ |
| Specific heat capacity | c | 0.728 J/(g·°C) |
| Heat conductivity coefficient | k | 1.35 W/(m·°C) |
| Relative dielectric constant | ϵ_r | 2.25 |
| Young modulus | E | 7.36×10^{10} (Pa) |
| Shear modulus | G | 3.14×10^{10} (Pa) |
| Compressive strength | P | 800~1000 (MPa) |
| Poisson’s ratio | ν | 0.17 |

Table 2. Thermodynamic parameters of various impurity defects used in the calculation [40–42].

| Defect Species | Density (g/cm ³) | Specific Heat Capacity (J/(g·°C)) | Heat Conductivity (W/(cm·°C)) | Coefficient of Linear Expansion ($\times 10^{-6} \text{ K}^{-1}$) | Young Modulus (GPa) | Poisson’s Ratio |
|------------------|------------------------------|-----------------------------------|-------------------------------|---|---------------------|-----------------|
| Fe | 7.0 | 0.45 | 0.565 | 11.8 | 152.0 | 0.30 |
| Al | 2.7 | 0.88 | 2.38 | 23.0 | 70.0 | 0.33 |
| CeO ₂ | 7.13 | 0.465 | 0.045 | 13.2 | 174 | 0.32 |

Figure 1 shows the FEM model for simulating the temperature and thermal stress distributions caused by subsurface impurity defect. To improve the computational efficiency, only the domain exposed within the laser spot is calculated and the diameter of fused silica is set to be 400 μm . The sample thickness is chosen as 10 μm due to the dramatically attenuating of laser energy in the vertical propagation direction. A two-dimensional axisymmetric finite element model is applied in this work for a cylindrical fused silica optics. The diabatic boundary conditions combined with the surface-to-ambient radiation boundary are applied at the borders of the simulation domain. Since the energy of the applied incident lasers is spatially distributed with a Gaussian profile, the temperature in the area beyond the laser spot would be much lower than those in the central area. Hence, the applied boundary conditions would not affect the simulation accuracy and more attention should be paid on the results of temperature and stress fields near the central area. The laser parameters chosen in the simulations are the same as those applied in the actual laser damage experiments to ensure accurate and reliable simulation results. It is worth noting that the actual laser energy is spatially distributed with an approximate Gaussian distribution. For simplicity, the spatial distribution of incident lasers with Gaussian shape (see Figure 1c) is applied in the simulations with a 390- μm beam diameter and a 10-ns pulse duration. The laser frequency is 1 Hz and after each laser pulse the fused silica sample cools down naturally. In this work, the evolutions of temperature and stress distributions during the laser heating and free cooling processes are both simulated and the total simulation running time is set to be much longer than the pulse duration to insure the stable temperature and stress fields to be reached finally. For simplicity, the impurity defect inside fused silica in Figure 1b is viewed as a small spherical particle positioned right beneath the laser spot center. The simulation domain is non-uniformly gridded in different regions: the defect region is gridded with triangular mesh, while the other region is gridded with quadrilateral mesh. Further, the refined gridding sizes are applied in the vicinity of fused silica-defect interface to guarantee the simulation accuracy. We have adjusted the maximum element mesh size to check the deviations of the simulation results. It has been found that the simulation results with the applied mesh sizes are maintained almost equal to those with more refined meshes, which indicates that the mesh generation is applicable to the simulations.

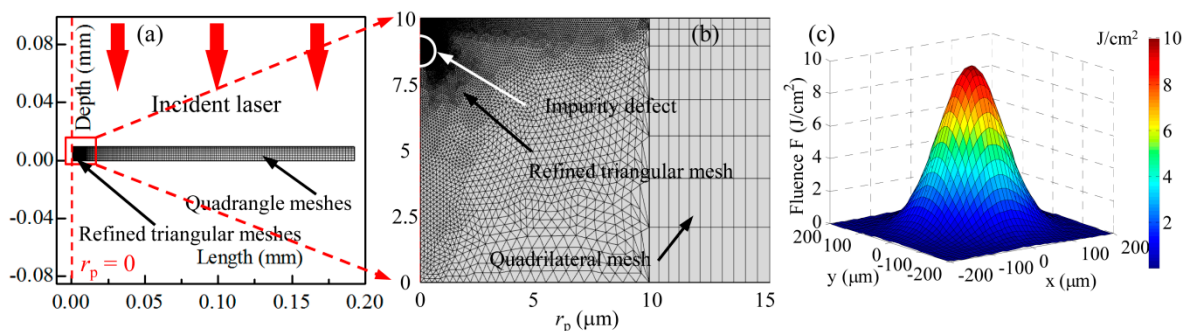


Figure 1. The finite element method (FEM) model for simulating the temperature and thermal stress distributions initiated by impurity defects under intense laser irradiation: (a) the FEM model; (b) the designed gridding; (c) the spatial energy distribution of applied Gaussian laser pulse.

2.2. Sample Preparation, SSD Removal, and Etching Process Characterization

In the practical chemical-mechanical polishing process of fused silica optics, mechanical and chemical actions are both involved in generating the polished surfaces by mutual contact, friction, squeezing and deformation between polishing agent and optical surface. Under the combined work of mechanical and chemical actions, the optical materials are removed, leaving the subsurface damage (SSD) distributed beneath the polished surface. The SSD distribution profile is presented in Figure 2, which includes re-deposition, defect and deformed layers [17,26,31,43]. The re-deposition layer consists of impurity defects and silica compounds, resulting from the hydrolysis reaction of fused silica.

The defect layer is mainly formed by cracks and scratches introduced in the initial rough grinding process. Besides, in the final polishing process, the impurity defects are easily imbedded and hidden inside the defect layer as well. The deformed layer is generated by the deformation of optical materials, which ascribes to the pressure stress of grinding wheel and buffing pad in the processing processes.

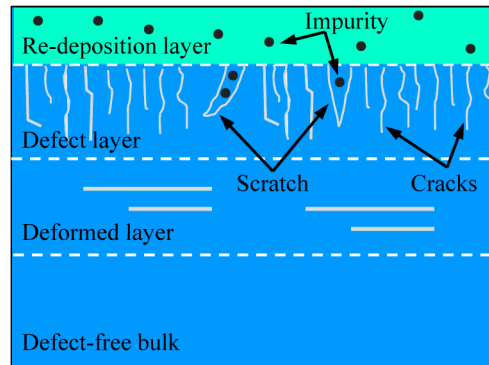


Figure 2. Schematic of the subsurface damage (SSD) defect distribution located beneath the ground and polished fused silica surface.

To promote the laser damage resistance of fused silica optics, the HF acid etching technique is employed in this work to remove the subsurface impurity defects. In the etching process, the topside re-deposition layer including most of the impurity defects is firstly dissolved by chemical reaction between the HF acid and hydrolysis products. Then, the crack and scratch defects are blunted and the embedded impurity can be also easily wiped off. In this way, the detrimental impact of these SSD defects on the laser damage resistance can be greatly mitigated for the silica optics. In the sample preparing process, W14-sized SiC abrasive particles are adopted to grind the ten pieces of initial fused silica samples (30-mm diameter and 5-mm thickness) for half an hour. The ground samples are then polished for 2 h with 1- μm -diameter CeO₂ polishing slurry to ensure that large brittle scratches and cracks are totally removed or buried under the re-deposition layer. The grinding and polishing spindle speeds are 50 r/min and 40 r/min. The grinding and polishing solution concentrations are 10 wt % and 8 wt %, respectively, with a 22-kPa load pressure. Figure 3 shows the HF acid etching schematic for removing the subsurface impurity defects. The HF-based etchant with 2% HF (mass fraction) and 5% NH₄F (mass fraction) is applied with solvent of deionized water. The NH₄F solvent, regarded as buffered oxide etch (BOE), is added in the etching process to promote the F⁻ population and eventually guarantee the stable etching rate and low evaporation pressure. It should be noted that one half side of the topmost sample surface is set as reference with the paraffin applied over it to prevent the acid etching. Meanwhile, the other half side of the polished silica surface is etched when submerged into the HF-based etchant. After different periods of acid etching, the samples are cleaned with deionized water and the coated paraffin layers are removed with acetone reagent. The effectiveness of acid etching on removing the subsurface defects of polished silica optics is presented by the etching depths at various etching times, which can be directly calculated from a key parameter of etching rate. The etching rate in this work is measured with a stylus profilometer and the principle diagram of the measuring process is shown in Figure 3b. For silica samples etched for various periods, the profilometer stylus scans perpendicularly to the dividing line of the un-etched and etched surfaces to obtain the height profiles before and after HF acid etching. By comparing the height profiles of the two surface regions, the etching depths under various etching periods can be calculated, and the curve of etching rate is then accordingly achieved as well (see Figure 3b).

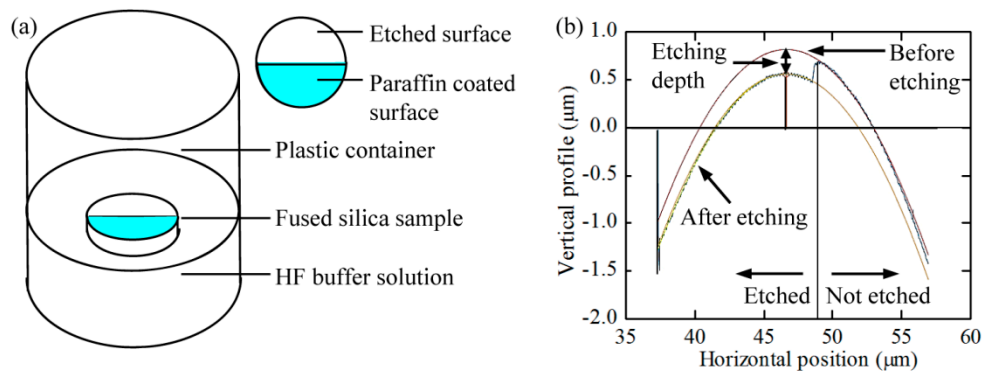


Figure 3. Sketch of the HF acid etching experiment (a) and the principle diagram; (b) for determining the etching depth using stylus profilometer in the etching process of fused silica optics.

Besides, in order to investigate the dynamic evolution of the surface quality involved in the etching process, the surface roughness and morphology are both tested at various etching times using a 3D stereo microscope, white light interferometer and profilometer. To quantitatively characterize the effectiveness of HF-based etching on eliminating the subsurface impurities, an energy dispersive X-ray spectrometer (EDS) is employed to test and compare the amounts of impurity defects before and after the acid etching process.

2.3. Laser Damage Test

The laser-induced damage thresholds (LIDTs) of fused silica optics before and after HF acid etching are measured following R-on-1 test protocol to validate the effect of impurity on laser damage resistance. In this test protocol, the laser pulse with fluence far below the damage threshold is initially applied. Then, incident lasers with pulse fluence increasingly ramped up are adopted until damage is observed. The LIDT is defined as the lowest fluence at which the damage occurs [44]. The laser damage experiment is carried out using a Q-switched Nd: YAG pump lasers (SGR-Extra-10, provided by the Beamtech Company (Beijing, China)). It is capable of steadily providing 1064 nm and 532 nm wavelength lasers with a 1-Hz repetition rate and 10-ns pulse width. The detailed parameters of the laser damage test are listed in Table 3.

Table 3. The experimental parameters for laser damage test on fused silica.

| Pulse Width τ_p /ns | Wavelength λ /nm | Repetition Rate ν /Hz | Beam Diameter D /µm | Incident Angle θ_i /deg | Laser Modal | Divergence Angle θ_d /mrad |
|-----------------------------|-----------------------------|------------------------------|--------------------------|-----------------------------------|-------------------|--------------------------------------|
| 10 | 355 | 1 | 390 | 0 | TEM ₀₀ | ≤2.5 |

The setup used to test the LIDT of fused silica is sketched in Figure 4. The pump laser is effectively delivered and focused on the surface of tested fused silica sample by propagating through focusing lens, wedged splitter and reflection mirrors. The attenuator consisting of polarizer and half-wave plate is used to adjust the energy output of the laser system. The pulse energy of each laser shot is calculated and recorded by monitoring the partial light energy, split from the main pump lasers using a wedged splitter. The sample is firmly mounted on the 3D translation stage to assure its position is accurately adjusted during the laser damage test. The judgment of the laser damage initiation is crucial to the laser damage test in that the measured LIDT is directly determined by the laser energy at which the laser damage is initiated. The Normaski microscope camera with magnification ranging from 100 to 200 times is employed to image any permanent changes (i.e., laser-induced damage) on the tested sample surface. Furthermore, the laser damage morphology is also real-time monitored with a He-Ne laser scattering system as shown in Figure 4b. By travelling through the focus lens, the He-Ne probe lasers scattered from the tested surface can be focused on the photoelectric detector. The detector

linked with a phase-locked amplifier is capable of recognizing the weak scattering light signal. When the laser damage is initiated on the tested surface, the signal becomes stronger. As a result, the laser damage can be precisely judged by real-time monitoring the change of the scattering light signal.

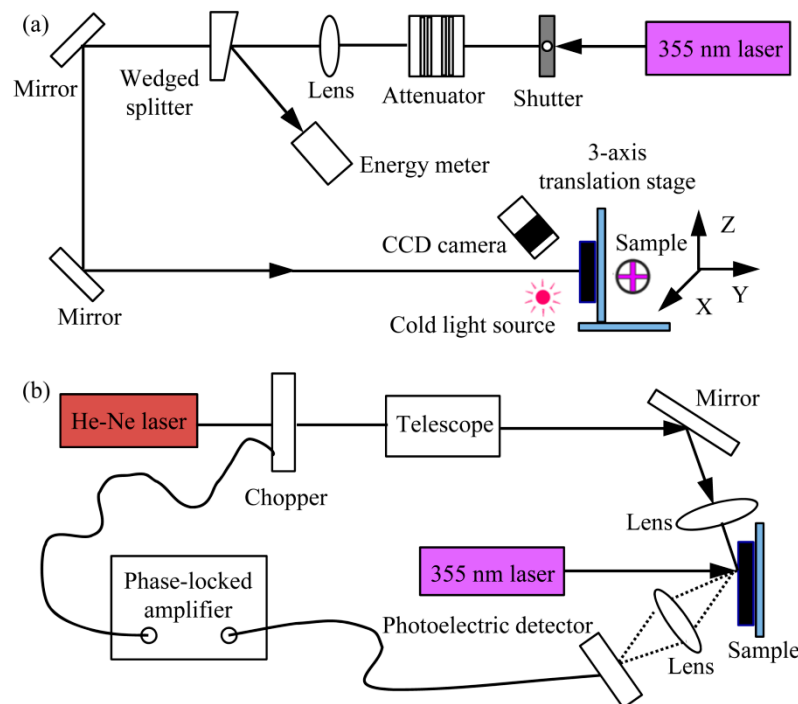


Figure 4. Schematic diagram of the laser path designed for the laser damage experiments (a) and the online monitoring system; (b) applied for detecting the laser damage initiation.

3. Results and Discussion

3.1. Temperature Distribution Caused by the Subsurface Impurity Defects

3.1.1. Comparison of Temperature Distributions with and without Impurity Defects

Figure 5 shows the comparison of temperature distributions caused by fused silica optics with and without impurity defects under the irradiation of Gaussian laser pulse with a 355 nm wavelength, 10 ns pulse width and 10 J/cm² laser fluence. The typical subsurface impurity defects of CeO₂, Fe and Al are all considered with defect diameter of 1 μm that is located 1 μm (the distance between defect center and surface) beneath the optical surface. Figure 5a,b exhibits the temperature curves for fused silica without any impurity defect. It is shown that under the irradiation of Gaussian laser pulse, the temperature field on the silica surface is also distributed in a Gaussian profile. With the increase of laser loading time ($t < 10$ ns), the temperatures on the surface rise gradually, and the maximum temperature at the center of Gaussian profile ($r_p = 0$ mm) can reach the peak of 1650 K when the laser pulse lasts for 10 ns (pulse width). The peak temperature is lower than the melting point (2173 K) of fused silica so that no laser damage will occur under this condition. The evolution of peak temperature ($r_p = 0$ mm) in the heating ($t < 10$ ns) and cooling ($t > 10$ ns) phases is exhibited in Figure 5b. One can see that when the laser stops heating, the peak temperature will dramatically decrease. The temperature gradually falls down thereafter to a stable and low value at room temperature (~300 K), when the laser pulse ends for 10⁴ ns. It means that the simulated temperature field would reach a stable state finally. It should be noted that the central-point temperature in Figure 5b shows a short plateau from $t = 15$ ns to $t = 30$ ns and the potential explanation is listed below. After the laser ends ($t > 10$ ns), when the decreasing surface temperature is close to that in the bulk, the effects of convection and radiation of

the surface would make the surface temperature keep decreasing. The surface temperature would be then lower than that of the bulk, and the heat energy could be transferred from the bulk to the surface. Owing to the competitive contributions of natural convection, surface radiation and heat transfer, the central-point temperature may remain roughly a short constant.

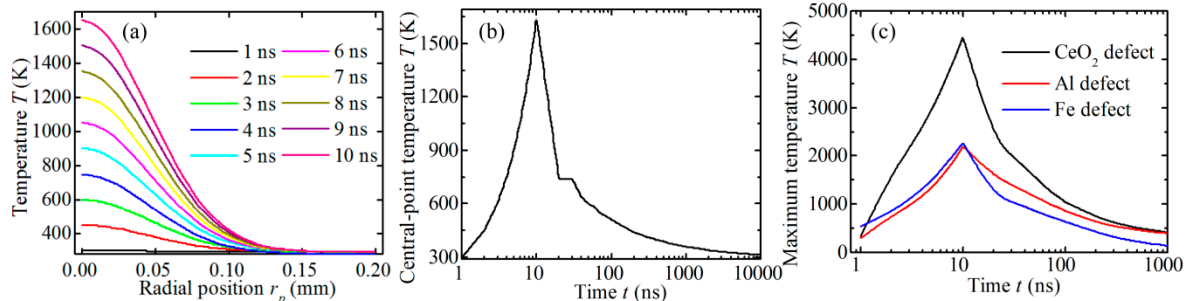


Figure 5. Comparison of temperature distributions caused by fused silica optics with and without impurity defects. (a) Temperature variation with respect to the radial position without impurity defect. Evolution of the peak temperature for fused silica optics without (b) and with (c) impurity defects of CeO₂, Al and Fe.

Figure 5c shows the variations of peak temperatures caused by impurity defects of CeO₂, Fe and Al. It can be seen that the peak temperature caused by CeO₂ defect rises more strongly than those caused by Fe and Al defects. The maximum temperature can reach 4458 K, which is much higher than the melting point of fused silica and the melting (2673 K) and boiling (3773 K) points of CeO₂. This means that the fused silica would be seriously damaged with the presence of a CeO₂ impurity defect. The maximum temperatures caused by Al and Fe impurity defects are both above 2200 K, which is also higher than the melting points of Al (933 K) and Fe (1808 K). Hence, the fused silica optics with Fe and Al impurity defects would also suffer from laser damage under the irradiation of an intense laser pulse. It can be concluded that with the presence of impurity defects, the optical materials would strongly absorb the laser energy, melt or even boil, and finally incur optical breakdown under the irradiation of a 355 nm wavelength, 10 ns pulse width and 10 J/cm² laser fluence.

The evolutions of temperature distributions caused by impurity defects are presented in Figure 6. As shown in Figure 6a–c, due to the strong absorption of CeO₂ defect, the temperature on the upper surface of impurity defect greatly increases in the heating process of laser pulse ($t < 10$ ns). When the laser pulse ends, the absorbed thermal energy is gradually diffused and transferred upward to the fused silica surface and downward to the bulk of the spherical CeO₂ defect. This means that the temperature distribution around the defect is non-symmetrical along the z -direction and should be highly dependent on their distances relative to the location of the initial incident lasers. Figure 6d,e shows the temperature distribution along the central axis for CeO₂ and Al defects at various times. One can see that, as the laser pulse acts, the temperature inside Al impurity defect (z -position ranging from 8.5 μm to 9.5 μm) becomes more and more uniform. The temperature is totally uniformly distributed in the bulk of Al defect when $t > 30$ ns (the curve keeps horizontally stable). However, for the case of the CeO₂ impurity defect, its induced temperature distribution inside impurity defect keeps barely uniform. The fact that the heat conduction capacity of Al is much better than that of CeO₂ should be responsible for this phenomenon.

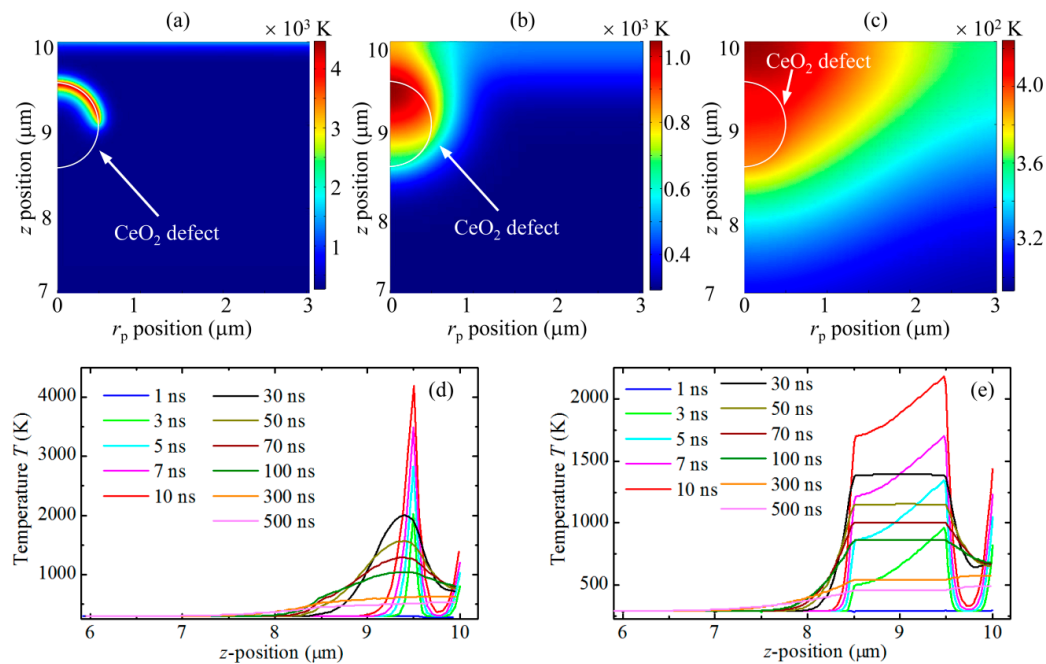


Figure 6. The temperature distributions on the longitudinal cross-section (z - r_p plane) caused by CeO_2 defect for laser loading times of (a) 10 ns; (b) 100 ns; (c) 1000 ns and (d) the temperature distributions along the central axis ($r_p = 0 \mu\text{m}$) caused by CeO_2 and Al (e) defects for various laser loading times.

3.1.2. Effect of Impurity Defect Parameters on Temperature Distribution

In order to figure out the most dangerous impurity defect to the laser damage resistance of fused silica, we investigate the temperature distributions caused by impurity defects with various structural parameters (e.g., defect radius r , defect depth d). The effect of defect structural parameters on its induced temperature rise is demonstrated in Figure 7. As shown in Figure 7a, after being exposed in lasers for 10 ns, the maximum temperatures caused by impurity defects ascend sharply and then decrease gradually with the increase of defect radius. The critical defect radius corresponding to the highest temperatures for Al and Fe impurity defects is $0.15 \mu\text{m}$. The highest temperatures are 3037 K and 2965 K, respectively, for the Al and Fe defects. Meanwhile, for the CeO_2 defect, the critical radius is $0.15 \mu\text{m}$ with the highest temperature of 4531 K. Temperature with this order of magnitude is high enough to incur matter evaporation, or even plasma formation, which would consequently induce local volume expansion, surrounding material fracture and finally laser damage. The phenomenon of maximum temperature evolution with respect to the defect radius can be explained as follows: as the defect radius increases, the defect area irradiated by incident lasers will enlarge, resulting in more laser energy to be absorbed by the defect. However, the enlarged irradiation area of impurity defect will increase the energy loss by thermal diffusion as well. Besides, with the increase of defect radius, the increase rate of absorbed energy would gradually decrease owing to the Gaussian distribution of the incident laser energy. Based on this, there must be a critical defect radius existing between the heat absorbing and diffusing processes, at which the temperature would reach the summit. This is consistent with the results shown in Figure 7a. Figure 7b shows the dynamic evolution of maximum temperature versus the defect radius. One can see that during the laser loading period ($t < 10 \text{ ns}$), the maximum temperature increases firstly and then decreases gradually similar to the results as shown in Figure 7a. When the laser pulse ends ($t > 10 \text{ ns}$), the temperature keeps rising all the time with the increase of defect radius. This is because under the same heat diffusing circumstance, an impurity defect with large size will hold more thermal energy and correspondingly induce a higher temperature. This agrees with the explanation discussed above. The simulation results at the loading times before ($t = 1 \text{ ns}, 3 \text{ ns}, 5 \text{ ns}, 7 \text{ ns}, 10 \text{ ns}$) and after ($t = 30 \text{ ns}, 50 \text{ ns}, 70 \text{ ns}, 100 \text{ ns}, 300 \text{ ns}$) the incident laser

heating process as shown in Figure 7b validate that the maximum temperatures caused by impurity defects with various radii generally take place at the ending time ($t = 10$ ns) of the laser pulse. Hence, the variations of maximum temperatures at $t = 10$ ns with respect to the defect radius and depth are summarized in Figure 7a,c to obtain the most dangerous impurity defects in the polished fused silica optics.

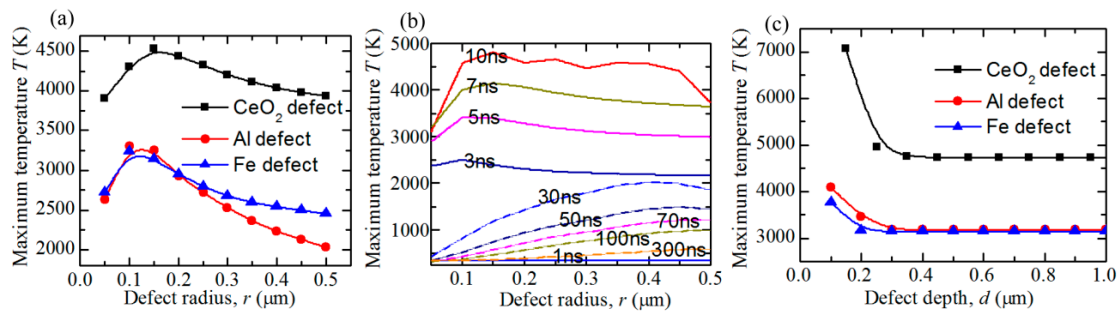


Figure 7. Evolutions of the maximum temperatures caused by various impurity defects with respect to the defect radius (a) and depth (c) during the laser loading period of 10 ns. (b) The dependence of maximum temperature on defect radius for CeO₂ defects under various laser loading times.

Figure 7c exhibits the dependence of maximum temperature on the defect depth. It is shown that the maximum temperature caused by impurity defect is higher when it is located more closely to the fused silica surface. When the defect depth is deeper than $0.3 \mu\text{m}$, the maximum temperature will keep constant as the defect depth increases. This is because the heat conductivity coefficient of ambient air ($0.023 \text{ W}\cdot\text{m}^{-1}\cdot\text{K}^{-1}$) is lower than that of fused silica materials. For defect located more closely to the surface, the thermal energy is more prone to transfer among the ambient air. Under this circumstance, less energy will be lost by thermal diffusion. Hence, the temperature is higher when the defect resides closer to the silica surface. However, when the defect is located deeper than $0.3 \mu\text{m}$ beneath the surface, the effect of ambient air on thermal diffusion becomes negligible. From the simulations of temperature distributions shown above, we can conclude that impurity defects (especially for CeO₂) located closer than $0.3 \mu\text{m}$ away from the surface with defect radius ranging from $0.1 \mu\text{m}$ to $0.15 \mu\text{m}$ are most dangerous defects for lowering the laser damage resistance of polished fused silica optics.

3.2. Thermal Stress Distribution Caused by the Subsurface Impurity Defects

3.2.1. Comparison of Thermal Stress Distributions with and without Impurity Defect

By numerically solving Equations (1) and (4) with finite element method (FEM), the physics of heat conduction and solid mechanics involved in the intense laser irradiation process can be well coupled for obtaining the thermal stress distribution caused by impurity defects. The thermal stress could be applied to describe the negative effect of impurity defects on the mechanical property and wavefront distortion of fused silica optics with high precision surfaces. In this section, the von Mises equivalent stress is employed to evaluating the yielding behavior of fused silica material with the presence of subsurface impurity defects. Figure 8 presents the comparison of von Mises equivalent stress on fused silica with and without impurity defects. The parameters of incident lasers are the same to those applied in Section 3.1 ($10 \text{ J}/\text{cm}^2$, 355 nm , 10 ns) and the defects of CeO₂, Fe and Al are all investigated with a $1 \mu\text{m}$ defect radius and a $1 \mu\text{m}$ defect depth. The negative effect of impurity defects on laser damage resistance of fused silica optics is primarily related to the maximum temperature and stress during the laser irradiating process. Hence, in this work, we only concentrate on the transient simulation results of the maximum temperature and stress, which generally take place at roughly 10 ns when the laser pulse ends.

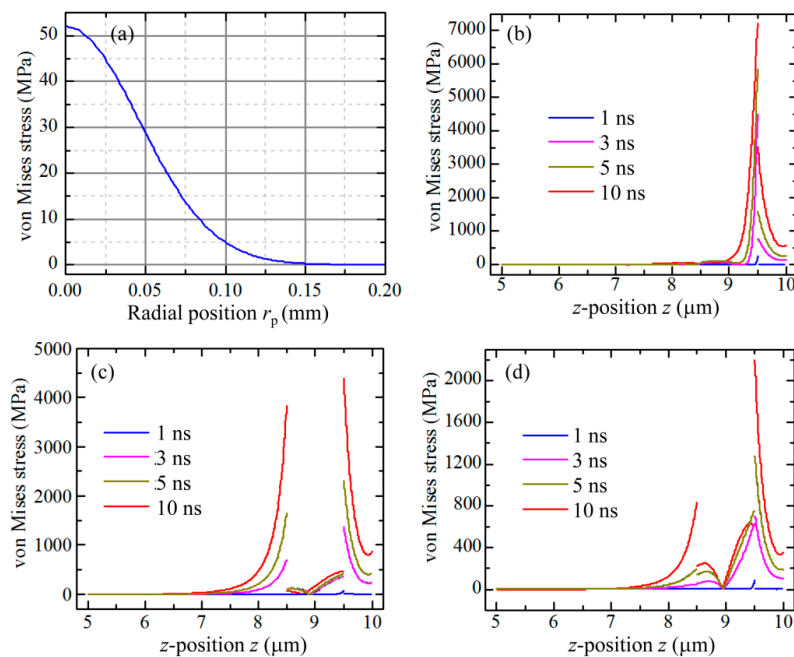


Figure 8. Comparison of the von Mises thermal stress distributions with and without impurity defects. (a) Thermal stress distribution along the radial direction ($z = 10 \mu\text{m}$) on fused silica surface without impurity defect. The maximum stress at $r_p = 0 \mu\text{m}$ could be applied in the comparison with those caused by the impurity defects. The von Mises thermal stress distribution along the central axis ($r_p = 0 \mu\text{m}$) caused by (b) CeO_2 ; (c) Al and (d) Fe defects for various laser loading times. The z -positions of $8.5 \mu\text{m}$ and $9.5 \mu\text{m}$ are the intersection points of fused silica with the downmost and upmost parts of the impurity defect.

As shown in Figure 8a, for fused silica optics without a subsurface defect, the induced von Mises stress appears in standard Gaussian distribution under the laser irradiation. The maximum thermal stress is 52 MPa, which is far lower than the strength of fused silica (800–1000 MPa). It means that the mechanical property and surface deformation of fused silica would be not strongly affected under the laser irradiation with this level of power. For the thermal stress in fused silica optics with impurity defects, it is demonstrated in Figure 8b–d that different types of impurity defects can induce different thermal stress distribution under the intense laser irradiation. The highest thermal stress is induced by the CeO_2 impurity defect, followed by Al and Fe defects. The maximum von Mises equivalent thermal stress induced by CeO_2 defect is 7432 MPa located on the topmost surface of defect and the maximum stress on the fused silica material is 3617 MPa. For Al and Fe defects, the induced maximum Mises equivalent thermal stresses are 4476 MPa and 2236 MPa, respectively. By comparing the simulated thermal stress distributions and thermodynamic parameters of Al and Fe defects, one can see that the coefficient of thermal expansion plays a dominant role in producing the higher thermal stress. It is also shown in Figure 8c,d that sharp changes exist at the intersections of fused silica material and impurity defect in the evolutions of von Mises stress caused by Al and Fe defects (the thermal stress curves have discontinuous points at z -positions of $8.5 \mu\text{m}$ and $9.5 \mu\text{m}$). This phenomenon can be explained below: (1) under the intense laser irradiation, the temperature rise of the impurity defect is greater than that of surrounding fused silica material and the local concentrated thermal load may be formed; (2) the thermal expansion coefficient of fused silica is much smaller than that of impurity defects that the impurity defect undergoing thermal expansion would be spatially constrained by the local surrounding silica materials; and (3) a big difference exists in the rigidity property of neighboring FEM elements due to the natural mechanical properties of the involved materials. However, for CeO_2 defect as shown in Figure 8b, since the thermal energy has been not already transferred to the downmost part (z -position of $8.5 \mu\text{m}$) of impurity defect, the temperature

rise in this region is very small. Besides, the CeO_2 defect and fused silica materials share a similar thermal expansion coefficient. Thus, for CeO_2 defect, the thermal stress curve at the lower intersection point of fused silica and impurity defect (z -position of $8.5 \mu\text{m}$) behaves continuously. While for the upper intersection point (z -position of $9.5 \mu\text{m}$), the temperature of impurity defect is much higher than that of fused silica. Under this situation, an obvious heat load would be probably formed, resulting in evident thermal stress discontinuity as shown in Figure 8b. It can be concluded that the impurity defect would lower the laser damage resistance of fused silica optics by its induced thermal expansion and stress. The thermal stress of impurity defect may incur high stress in the surrounding silica materials, which would exceed the compressive strength of fused silica optics and finally lead to its fracture and breakdown.

3.2.2. Effect of Impurity Defect Parameters on Its Induced Thermal Stress

In order to discern the most dangerous impurity defect to the laser damage resistance of fused silica optics, we also investigate the von Mises thermal stress caused by impurity defects with various structural parameters (e.g., defect radius r , defect depth d). Since the CeO_2 impurity defect would induce the highest temperature and thermal stress as discussed above, here we only consider the effect of CeO_2 defect parameters on its induced thermal stress, which is shown in Figure 9. As shown in Figure 9a, with the increase of defect radius, the von Mises stress ascends firstly and then decreases gradually. The maximum thermal stress reaches the summit (7420 MPa) when the defect radius is $0.15 \mu\text{m}$ (critical defect radius). One can see from Figure 9b that impurity defect located more closely to the silica surface would induce higher maximum thermal stress. The peak maximum stress of fused silica is 8739 MPa, and when the defect depth is larger than $0.3 \mu\text{m}$, it remains roughly stable. The changing tendency of maximum thermal stress with respect to defect parameters is similar to that of maximum temperature shown in Figure 7. It is worth noting that the thermal stress of fused silica is higher than that of CeO_2 defect as shown in Figure 9b. This is because the defect radius is so small (r keeps constant at the critical radius of $0.15 \mu\text{m}$) that the heat energy can be promptly transferred to the surrounding fused silica materials. As a result, fused silica with higher heat capacity would induce higher thermal stress.

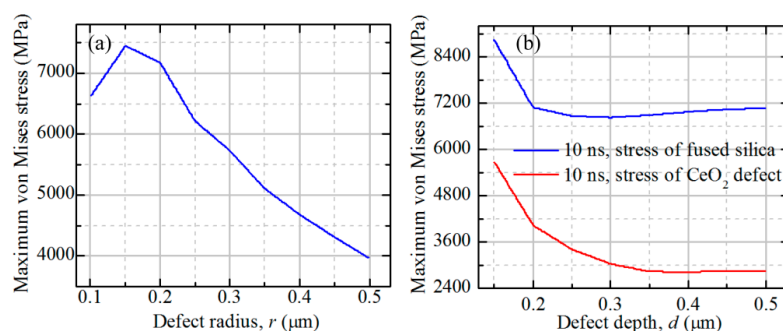


Figure 9. Evolution of the maximum von Mises stress caused by CeO_2 impurity defect with respect to the defect radius (a) and depth (b) when the fused silica surface is irradiated by incident lasers for 10 ns. The maximum thermal stresses in fused silica and CeO_2 defect are both presented in (b).

From the simulation results of defect-induced temperature and thermal stress distributions discussed above, one can see that the transient local high temperature can be produced by heat absorbing of impurity defects under the irradiation of intense lasers. The extremely high temperature would trigger the plasma formation inside the impurity defect, result in material expansion, and finally initiate the fracture and breakdown of the surrounding silica materials. In addition, the huge thermal stress caused by the impurity defect far exceeds the intrinsic strength limit of the material, making the fused silica optics susceptible to be crushed down. Furthermore, in the actual process of intense laser irradiation, the high temperature and thermal stress caused by the impurity defect could act together,

leading to even worse damage of fused silica optics. Based on the results above, we can conclude that the temperature and thermal stress caused by impurity defects strongly depends on the defect species and structural parameters. The CeO₂ defect can induce higher temperature and thermal stress than Al and Fe defects, especially when it is located more closely to the silica surface. The most dangerous subsurface impurity defect is the CeO₂ defect with a diameter of 0.3 μm, located less than 0.15 μm beneath the surface, which would induce local temperature up to 7073 K and von Mises equivalent thermal stress up to 8739 MPa. Therefore, we should pay close attention to control and remove this dangerous kind of subsurface defects in the practical manufacturing process of fused silica optics with high precision surfaces. By considering the synthetic effects of temperature and thermal stress caused by impurity defects, it can be concluded from the simulation results shown in Figures 8b–d and 7 that the CeO₂ defect plays the dominant role in decreasing the laser damage resistance of fused silica, followed by Al and Fe defects. It has been also experimentally observed by Neauport et al. [17,25] that the laser damage density of silica optics is most closely correlated to the cerium content, followed by Al and Fe defects. The correlation coefficients of damage density to the Ce, Al and Fe impurity defects are 0.99, 0.16 and 0.001, respectively. Hence, the simulation results of temperature and stress in this work are qualitatively supported by the previously experimental results and the present results would offer potential theoretical explanations on the experimental observations of the effect of impurity defects on the laser damage resistance of fused silica optics.

3.3. Removal of Subsurface Impurity Defects by HF Acid Etching

The simulation results of temperature and thermal stress caused by subsurface impurity defects presented in Sections 3.1 and 3.2 indicate that the impurity defects included in the SSD lasers play a crucial role in lowering the laser damage resistance of polished fused silica. In order to improve the laser damage resistance of silica optics, HF acid etching assisted with buffered oxide etch (BOE) is applied to remove the SSD layers. Then, the etching rate, surface quality and impurity contents are all investigated, and the laser damage threshold is tested to validate the effect of impurity defects on the laser damage resistance of fused silica optics.

3.3.1. Etching Rate of Fused Silica

Figure 10 presents the measured variation of etching rate as a function of etching time and etching depth using a stylus profilometer on the basis of a test scheme shown in Figure 3. One can see that in the initial etching process, the etching rate exhibits a sharp decrease from 46.45 nm/min to 28.81 nm/min. As the etching proceeds, the etching rate gradually descends to 23 nm/min and remains roughly stable. This phenomenon can be ascribed to the different speeds of chemical reaction of HF acid with body material (SiO₂) and hydrolysis product in form of hydrated silica gel (≡Si–OH). The product of hydrated silica gel is formed following the process below:

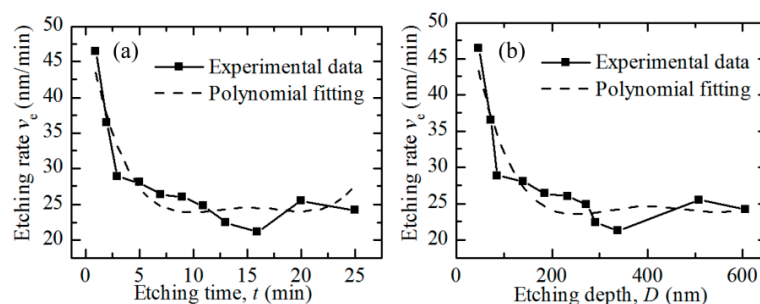


Figure 10. The evolution of etching rate with respect to the etching time (a) and etching depth (b).

Besides, the re-deposition layer produced in the grinding and polishing processes has a loose structure, which would enlarge its contact area with BOE and acid solvents. Hence, the etching rate appears very large in the initial etching phase. However, the curve shows a downtrend behavior because of the decreasing concentration of hydrated silica gel as the etching proceeds. When the re-deposition layer is totally removed, and the pure substrate of fused silica is exposed to the HF-based solvent, the etching rate would change slightly and keep almost constant as shown in Figure 10. Owing to the random motions of grinding and polishing particles, the density and depth of SSD defects on fused silica optics are somewhat different, even though the same processing parameters are applied. For this reason, the etching rate fluctuates with 10% amplitude in the steady etching process as shown in Figure 10. By polynomial fitting the etching rate data, we can conclude that a 200-nm etching depth and an 8-min etching time are required for steadily etching the SSD layers of polished silica optics. Based on the aforementioned discussions, it can be also inferred that the thickness of ground and polished silica optics is roughly 200 nm, which is consistent with most of the previously reported experimental results [24,26,45].

3.3.2. Surface Quality and Impurity Content of Fused Silica Etched by HF Acid

As the HF acid etching proceeds, not only the impurity defects included in the re-deposition layers are removed, but the subsurface cracks and scratches are blunted [26,27]. The optical quality of etched fused silica surfaces would have great changes and the surface roughness value is an important index in evaluating the quality of optical surface. Thus, the evolution of surface roughness value as the HF acid etching proceeds is investigated using the white light interferometer and profilometer to check the effect of acid etching on the surface quality. Figure 11 shows the tested evolution of surface roughness with respect to the etching time (or etching depth) for fused silica etched with HF-based solvent (5% HF and 10% NH_4F). It is shown that the surface roughness value R_a experiences three changing phases as the HF etching proceeds. During phase 1 with the etching depth smaller than 500 nm, the R_a ascends from 2.6 nm to 4.2 nm. The decrease of surface quality (rise of roughness) arises from the appearance of subsurface plastic scratches and cracks as the topmost re-deposition layers are removed. During phase 2 with the etching depth ranging from 0.5 μm to 2.15 μm , the R_a value descends from 4.2 nm to 3.3 nm due to the passivation of subsurface damage under the assistance of acid etchants. The subsurface cracks and scratches are etched and blunted, resulting in the improvement of surface quality. The surface roughness increases again during phase 3 for etching depth larger than 2.15 μm . The reproduction of scratches and opening of cracks with the increase of etching depth should be responsible for this results.

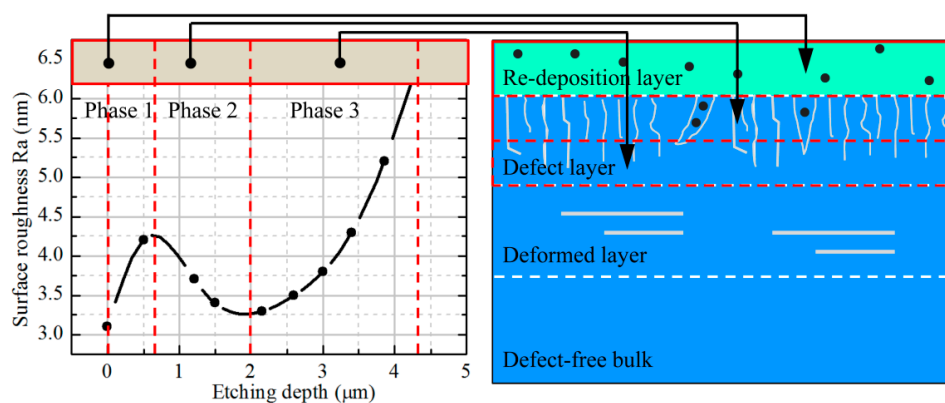


Figure 11. The evolution of surface roughness of etched fused silica optics as the acid etching proceeds and its corresponding etching depths.

Figure 12 presents the evolution of surface morphology of etched fused silica with various etching periods, which are tested by a 3D stereo microscope and white light interferometer. It can be seen

that with the increase of etching period, the subsurface defects (e.g., scratches, cracks, pits and so on) emerge and the defect population become larger. This is the further evidence for the great decrease of surface quality during phase 3 as shown in Figure 11. It should be noted that with a mixed etchant of 5% HF and 10% NH_4F , as applied in Figure 12, the re-deposition layer is totally removed when the etching period is 3 min. Thus, all of the tested surface morphology in Figure 12 corresponds to phase 3 shown in Figure 11.

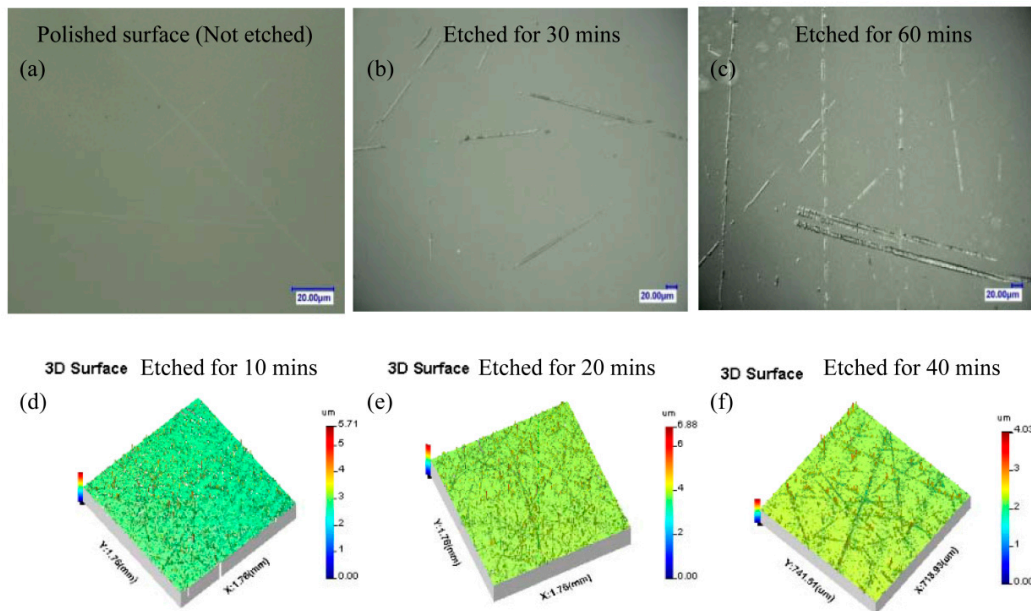


Figure 12. The evolution of surface morphology of etched fused silica under various etching periods. The etched surfaces are tested with a 3D stereo microscope for etching periods of (a) 0 min; (b) 30 min and (c) 60 min. The surface morphologies of etched surfaces are also tested with white light interferometer for etching periods of (d) 10 min; (e) 20 min and (f) 40 min.

To quantitatively evaluate the effectiveness of HF-based acid etching in removing the subsurface impurity defects, the comparison of defect contents on fused silica surfaces before and after acid etching is investigated using energy dispersive X-ray spectrometer (EDS). Figure 13 shows the comparison of defect content and the evolution of Ce content with the increase of etching time. For the defect content before acid etching as shown in Figure 13a, one can see that the contents of Si and O are two types of elements most distributed on the polished silica surface. They originate from the body material of fused silica (SiO_2) and satisfy their proportional relationship of mass fraction. Besides Si and O, other impurity defects (e.g., Ce, Fe, Cu and Se) are also observed with the maximum defect content of 7.45 wt % for Ce impurity. The results obtained in Section 3.1 and 3.2 indicate that the CeO_2 impurity defect plays the dominant role in lowering the laser damage resistance of polished fused silica optics. Hence, we take Ce defect as an example to investigate its elimination when the SSD layers of silica optics are etched with HF etchant. The tested impurity contents on etched silica surfaces are presented in Figure 13b. It is shown that the contents of most of the impurity defects are effectively lowered by acid etching, especially for the Ce impurity defect, whose content largely descends from 7.45 wt % to 3.24 wt %. It means that 56.5% of the CeO_2 impurity defects could be removed by HF acid etching and the heat absorption caused by impurity defects would be greatly mitigated to improve the laser damage resistance of fused silica. The evolution of Ce defect content with respect to the etching time is exhibited in Figure 13c. It can be seen that the content of Ce defect decreases gradually and becomes roughly stable when the fused silica optics are etched for a sufficient time. This phenomenon can be explained as follows. In the initial etching stage, the defect content decreases dramatically due to the removal of re-deposition layers, among which a majority of impurity defects are located and

distributed. After etching for 10 min, when the re-deposition layers are totally removed, the subsurface scratches and cracks appear and some of the impurity defects hidden inside or adsorbed to the cracks could be removed and washed away. The defect content therefore shows gradual decrease for etching time from 10 min to 50 min. When the silica optics are etched for longer than 50 min, the defect content keeps almost constant since the impurity defects adsorbed to the cracks are then difficult to be removed by ordinary etchant washing. From the discussions above, it can be concluded that the impurity defects can be effectively removed by HF-based acid etching. The acid etching shows the best effectiveness in removing the impurity defects, when the re-deposition layers are being etched. The mechanical properties and laser damage resistance of fused silica would be greatly improved by controlling the heat absorption caused by these impurity defects.

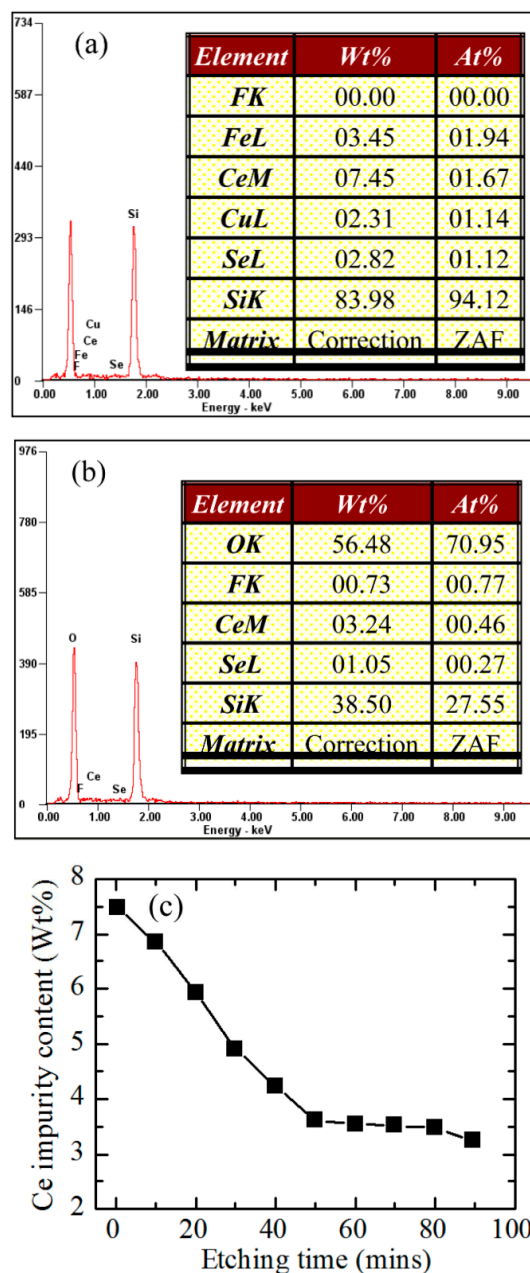


Figure 13. Tested results of impurity defects on polished silica surfaces before and after acid etching: (a) impurity contents before HF acid etching; (b) impurity contents after HF acid etching for 90 min; (c) Variation of Ce defect content for various etching times.

3.3.3. Laser Damage Resistance of Etched Fused Silica Surface

Now that the contents of impurity defects are effectively controlled, another key index, laser-induced damage threshold (LIDT) of etched fused silica optics should be checked as well. The LIDTs of fused silica etched for various times using etchant of 5% HF and 10% NH_4F are measured with the testing protocol and setup described in Section 2.3. A 10-min step of etching period is chosen in the HF-etching procedure and the reason as follows. Firstly, it can be derived from Figure 10 that an 8-min etching period and a 200 nm etching depth are required to ensure a steady etching rate for the polished fused silica optics with SSD layers. It means that the impurity defects mainly distributed among the uppermost re-deposition layer could be effectively removed within 10 min. Besides, the general trend of the tested Ce impurity content shown in Figure 13c would be clearly recognized with an etching period of 10 min.

The tested LIDTs for various etching times are shown in Figure 14a. It can be seen that the LIDT rises firstly (etching for less than 10 min) and then gradually decreases (etching for more than 10 min) as the etching proceeds. It is indicated by the results in Figure 10 that the re-deposition layers containing most of the impurity defects and hydrolysis products are initially removed during the first 8-min etching times. Combined with the results shown in Figure 14a, one can conclude that not only the impurity defects are effectively removed, but the LIDT of etched fused silica optics could be enhanced from 24.4 J/cm^2 to 27.1 J/cm^2 (355 nm, 10 ns). However, when the re-deposition layers are fully removed, the LIDT presents gradual decrease as the etching proceeds due to the appearance of subsurface scratches and cracks. Based on this, in the practical etching process of fused silica optics, the etching time should be accurately and strictly controlled to prevent the appearing and deepening of subsurface cracks and scratches. The morphological comparisons of laser damage spots on un-etched and etched fused silica optics are exhibited in Figure 14b,c. It can be seen that the damage spot on an un-etched silica surface is very large, consisting of many local small and concentrated damage sites. Besides, the damaged silica materials are all peeled off. As for the damage spots on etched silica surfaces, they are very small and discretely distributed right on the surface scratches. The difference in laser damage morphology on etched and un-etched silica surfaces indicates that the un-etched surfaces possess more impurity defects, which are the main initiators for inducing serious optical damage. When the polished fused silica surfaces are etched by HF acid, the amounts of impurity defects are greatly reduced, and correspondingly the laser damage resistance of silica optics could be effectively improved. This is consistent with the tested results of impurity defect contents on etched and un-etched fused silica surfaces. The laser damage experiment directly validates the negative effect of impurity defects on the laser damage resistance of fused silica. Since the CeO_2 , Al and Fe impurity defects are very difficult to be separated from each other and a silica sample with a single impurity defect is difficult to prepare in actual experiments, the respective effects of single impurity defects on laser damage resistance of fused silica optics are hard to be directly and quantitatively validated. Furthermore, the transient temperature caused by absorptive impurity defects is very high and it only lasts for such a short time that experimentally acquiring the transient high temperature is quite a challenge. Thus, it is very difficult to detect the accurate temperature evolution on the laser-irradiated silica surface to directly justify the simulation results in this work. However, the experimental results of the laser damage test show that the impurity defects are probably the absorbing initiators that incur the laser damage event. This indirectly validates the simulation results that the much higher temperature and stress caused by impurity defects in comparison to defect-free surfaces are the potential underlying mechanisms for explaining the low laser damage threshold of polished fused silica optics.

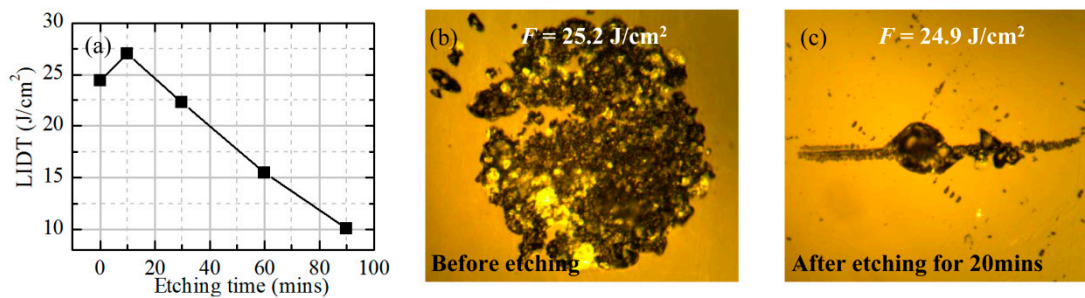


Figure 14. Comparison of the laser damage performance for fused silica optics before and after HF etching. (a) Variation of laser-induced damage thresholds (LIDTs) of etched silica surface under various etching times. The typical laser damage morphologies on un-etched (b) and etched (c) silica surfaces. The microscopic images in (b,c) are both magnified by 40 times.

The decrease of LIDT as shown in Figure 14a and the initiation of laser damage shown in Figure 14c should be blamed for the appearance of subsurface cracks and scratches. To solve this issue, two other parallel processing techniques, CO₂ laser conditioning [8] and thermal annealing [9,10], have been also being developed to close and heal the cracks and scratches by heat softening for mitigating the negative effect of subsurface defects, which is beyond the scope of the present work. It is worth noting that though the amount of CeO₂ defects as shown in Figure 13 can be reduced by more than a half, some residual impurity defects are still adsorbed on the etched surfaces or hidden beneath the subsurface cracks. The residual impurity defects would limit the capacity of the HF-based acid etching technique in promoting the laser damage resistance of fused silica optics. Therefore, based on HF-based etching, some new techniques (e.g., assistance of megasonic agitation and addition of chelating agent adoption) are being explored and developed to further remove the subsurface impurity defects of fused silica optics. In the experiments, the variation of the impurity defect population with respect to the increase of etching time is indirectly derived by characterizing the etching rate, impurity element content, laser damage threshold, surface roughness and morphology of etched silica surfaces. The errors in the etching process would bring in potential deviations of these characterized features to the actual case. Hence, the simulation results of the negative effects of impurity defects have been not quantitatively and accurately validated, and new techniques of testing the transient high temperature and analyzing the exact impurity defect content should be developed in the future to further justify the role of impurity defects in decreasing the laser damage resistance of the polished fused silica optics.

4. Conclusions

To evaluate the effects of impurity defects on the laser damage resistance of fused silica, the distributions of temperature and thermal stress caused by absorptive defects are investigated by numerically solving the heat conduction and thermo-elastic equations involved in the laser irradiation process. The simulation results indicate that the presence of impurity defects would induce a dramatic rise in temperature and thermal stress. The maximum temperature and thermal stress in fused silica can exceed its melting point and compressive strength, resulting in optical breakdown of optical materials. The effect of impurity defects on the laser damage resistance is dependent on the species, size and spatial position of defects. The CeO₂ defect plays the dominant role in lowering the laser damage resistance, followed by Fe and Al defects. The defects located more closely to the silica surfaces would incur higher local temperature. It is further concluded that the CeO₂ defects with radius of roughly 0.3 μm, which reside 0.15 μm beneath the silica surfaces, are the most dangerous defects affecting the laser damage resistance of fused silica optics.

With the HF-based etching method, the impurity defects on fused silica are removed and the surface quality, defect content and laser damage threshold of etched surfaces are experimentally tested to evaluate the etching effectiveness. The results show that the negative effect of impurity defects

on the laser damage resistance can be effectively mitigated by HF acid etching. As the acid etching proceeds, the re-deposition and subsurface defect layers are successively removed, resulting in the evolution of surface roughness in three phases. The EDS and laser damage experiments validate that the number of dangerous CeO₂ defects on fused silica can be decreased by more than a half and the LIDT can be improved to 27.1 J/cm² (355 nm, 10 ns) by removing the re-deposition layers. It is proved that the HF-based acid etching is able to effectively control the bad effect of impurity defects on the laser damage resistance and the further improvement of LIDT is limited by the deep scratches and cracks. This work can not only contribute to the understanding of laser-induced damage mechanisms on large-aperture ultraviolet optical components, but also provide theoretical foundations for the post-processing of ultra-precision machined fused silica optics.

Acknowledgments: The authors gratefully acknowledge the financial support from the Science Challenge Project (Grant No. JCKY2016212A506-0503) and the Key Laboratory Fund of Ultra-precision Machining Technology at the China Academy of Engineering Physics (Grant No. KF14007).

Author Contributions: Jian Cheng and Jinghe Wang conceived the work and supervised the preparation of the manuscript. Jian Cheng, Lei Zhang and Jing Hou performed the FEM simulations and analyzed the data. Jian Cheng, Jinghe Wang and Hongxiang Wang designed the experiments of acid etching and laser damage tests. Jian Cheng, Jing Hou, Lei Zhang and Hongxiang Wang fabricated and characterized the sample surfaces. Jian Cheng wrote the manuscript with the input from other coauthors. All authors reviewed the manuscript.

Conflicts of Interest: The authors declare no conflict of interest.

References

1. Stolz, C.J. The National Ignition Facility: The path to a carbon-free energy future. *Philos. Trans. R. Soc. A* **2012**, *370*, 4115–4129. [[CrossRef](#)] [[PubMed](#)]
2. Hurricane, O.A.; Callahan, D.A.; Casey, D.T.; Celliers, P.M.; Cerjan, C.; Dewald, E.L.; Dittrich, T.R.; Döppner, T.; Hinkel, D.E.; Berzak Hopkins, L.F.; et al. Fuel gain exceeding unity in an inertially confined fusion implosion. *Nature* **2014**, *506*, 343–348. [[CrossRef](#)] [[PubMed](#)]
3. Casner, A.; Caillaud, T.; Darbon, S.; Duval, A.; Thfouin, I.; Jadaud, J.P.; LeBreton, J.P.; Reverdin, C.; Rosse, B.; Rosch, R.; et al. LMJ/PETAL laser facility: Overview and opportunities for laboratory astrophysics. *High Energy Density Phys.* **2015**, *17*, 2–11. [[CrossRef](#)]
4. Dunne, M. A high-power laser fusion facility for Europe. *Nat. Phys.* **2006**, *2*, 2–5. [[CrossRef](#)]
5. Zheng, W.; Wei, X.; Zhu, Q.; Jing, F.; Hu, D.; Su, J.; Zheng, K.; Yuan, X.; Zhou, H.; Dai, W.; et al. Laser performance of the SG-III laser facility. *High Power Laser Sci. Eng.* **2016**, *4*, e21. [[CrossRef](#)]
6. Campbell, J.H.; Hawley-Fedder, R.A.; Stolz, C.J.; Menapace, J.A.; Borden, M.R.; Whitman, P.K.; Yu, J.; Runkel, M.; Riley, M.O.; Feit, M.D.; et al. NIF optical materials and fabrication technologies: An overview. *Proc. SPIE* **2004**, *5341*, 84–101.
7. Baisden, P.A.; Atherton, L.J.; Hawley, R.A.; Land, T.A.; Menapace, J.A.; Miller, P.E.; Runkel, M.J.; Spaeth, M.L.; Stolz, C.J.; Suratwala, T.I.; et al. Large optics for the National Ignition Facility. *Fusion Sci. Technol.* **2016**, *69*, 295–351. [[CrossRef](#)]
8. Lamaignère, L.; Bercegol, H.; Bouchut, P.; Durning, A.; Néauport, J.; Piombini, H.; Razé, G. Enhanced optical damage resistance of fused silica surfaces using UV laser conditioning and CO₂ laser treatment. *Proc. SPIE* **2004**, *5448*, 952–960.
9. Raman, R.N.; Matthews, M.J.; Adams, J.J.; Demos, S.G. Monitoring annealing via CO₂ laser heating of defect populations on fused silica surfaces using photoluminescence microscopy. *Opt. Express* **2010**, *18*, 15207–15215. [[CrossRef](#)] [[PubMed](#)]
10. Raman, R.N.; Negres, R.A.; Matthews, M.J.; Carr, C.W. Effect of thermal anneal on growth behavior of laser-induced damage sites on the exit surface of fused silica. *Opt. Mater. Express* **2013**, *3*, 765–776. [[CrossRef](#)]
11. Smith, A.V.; Do, B.T. Picosecond-nanosecond bulk damage of fused silica at 1064 nm. *Proc. SPIE* **2008**, *7132*, 71321E.
12. Stäblein, J.; Pöhl, K.; Weisleder, A.; Gönnä, G.; Töpfer, T.; Hein, J.; Siebold, M. Optical properties of CaF₂ and Yb³⁺: CaF₂ for laser applications. *Proc. SPIE* **2011**, *8080*, 808002.
13. Azumi, M.; Nakahata, E. Study of relation between crystal structure and laser damage of Calcium Fluoride. *Proc. SPIE* **2010**, *7842*, 78421U.

14. Singh, N.B.; Suhre, D.R.; Balakrishna, V.; Marable, M.; Meyer, R. Far-infrared conversion materials: Gallium Selenide for far-infrared conversion application. *Prog. Cryst. Growth Charact. Mater.* **1998**, *37*, 47–102. [[CrossRef](#)]
15. DeYoreo, J.J.; Burnham, A.K.; Whitman, P.K. Developing KH_2PO_4 and KD_2PO_4 crystals for the world's most powerful laser. *Int. Mater. Rev.* **2002**, *47*, 113–152. [[CrossRef](#)]
16. Negres, R.A.; Zaitseva, N.P.; DeMange, P.; Demos, S.G. Expedited laser damage profiling of $\text{KD}_x\text{H}_{2-x}\text{PO}_4$ with respect to crystal growth parameters. *Opt. Lett.* **2006**, *31*, 3110–3112. [[CrossRef](#)] [[PubMed](#)]
17. Neauport, J.; Lamaignere, L.; Bercegol, H.; Pilon, F.; Birolleau, J.C. Polishing-induced contamination of fused silica optics and laser induced damage density at 351 nm. *Opt. Express* **2005**, *13*, 10163–10171. [[CrossRef](#)] [[PubMed](#)]
18. Papernov, S.; Schmid, A.W. Laser-induced surface damage of optical materials: Absorption sources, initiation, growth, and mitigation. *Proc. SPIE* **2008**, *7132*, 71321J.
19. Wang, J.; Li, Y.; Han, J.; Xu, Q.; Guo, Y. Evaluating subsurface damage in optical glasses. *J. Eur. Opt. Soc. Rapid Publ.* **2011**, *6*, 11001.
20. Camp, D.W.; Kozlowski, M.R.; Sheehan, L.M.; Nichols, M.; Dovik, M.; Raether, R.; Thomas, I. Subsurface damage and polishing compound affect the 355-nm laser damage threshold of fused silica surfaces. *Proc. SPIE* **1998**, *3244*, 356–364.
21. Feit, M.D.; Rubenchik, A.M. Influence of subsurface cracks on laser induced surface damage. *Proc. SPIE* **2004**, *5273*, 264–272.
22. Neauport, J.; Cormont, P.; Legros, P.; Ambard, C.; Destribats, J. Imaging subsurface damage of grinded fused silica optics by confocal fluorescence microscopy. *Opt. Express* **2009**, *17*, 3543–3554. [[CrossRef](#)] [[PubMed](#)]
23. Liu, H.; Huang, J.; Wang, F.; Zhou, X.; Jiang, X.; Dong, W.; Zheng, W. Photoluminescence defects on subsurface layer of fused silica and its effects on laser damage performance. *Proc. SPIE* **2015**, *9255*, 92553V.
24. Hu, G.; Zhao, Y.; Liu, X.; Li, D.; Xiao, Q.; Yi, K.; Shao, J. Combining wet etching and real-time damage event imaging to reveal the most dangerous laser damage initiator in fused silica. *Opt. Lett.* **2013**, *38*, 2632–2635. [[CrossRef](#)] [[PubMed](#)]
25. Neauport, J.; Cormont, P.; Lamaignère, L.; Ambard, C.; Pilon, F.; Bercegol, H. Concerning the impact of polishing induced contamination of fused silica optics on the laser-induced damage density at 351 nm. *Opt. Commun.* **2008**, *281*, 3802–3805. [[CrossRef](#)]
26. Suratwala, T.I.; Miller, P.E.; Bude, J.D.; Steele, W.A.; Shen, N.; Monticelli, M.V.; Feit, M.D.; Laurence, T.A.; Norton, M.A.; Carr, C.W.; et al. HF-based etching processes for improving laser damage resistance of fused silica optical surfaces. *J. Am. Ceram. Soc.* **2011**, *94*, 416–428. [[CrossRef](#)]
27. Ye, H.; Li, Y.; Yuan, Z.; Wang, J.; Yang, W.; Xu, Q. Laser induced damage characteristics of fused silica optics treated by wet chemical processes. *Appl. Surf. Sci.* **2015**, *357*, 498–505. [[CrossRef](#)]
28. Ye, H.; Li, Y.; Zhang, Q.; Wang, W.; Yuan, Z.; Wang, J.; Xu, Q. Post-processing of fused silica and its effects on damage resistance to nanosecond pulsed UV lasers. *Appl. Opt.* **2016**, *55*, 3017–3025. [[CrossRef](#)] [[PubMed](#)]
29. Stevens-Kalceff, M.A.; Wong, J. Distribution of defects induced in fused silica by ultraviolet laser pulses before and after treatment with a CO_2 laser. *J. Appl. Phys.* **2005**, *97*, 113519. [[CrossRef](#)]
30. Hrubesh, L.W.; Norton, M.A.; Molander, W.A.; Donohue, E.E.; Maricle, S.M.; Penetrante, B.M.; Brusasco, R.M.; Grundler, W.; Butler, J.A.; Carr, J.W.; et al. Methods for mitigating surface damage growth on NIF final optics. *Proc. SPIE* **2002**, *4679*, 23–33.
31. Menapace, J.A.; Davis, P.J.; Steele, W.A.; Wong, L.L.; Suratwala, T.I.; Miller, P.E. MRF applications: Measurement of process-dependent subsurface damage in optical materials using the MRF wedge technique. *Proc. SPIE* **2006**, *5991*, 599103.
32. Cormont, P.; Gallais, L.; Lamaignère, L.; Donval, T.; Rullier, J.L. Effect of CO_2 laser annealing on residual stress and on laser damage resistance for fused silica optics. *Proc. SPIE* **2010**, *7842*, 78422C.
33. Jiang, X.; Liu, Y.; Rao, H.; Fu, S. Improve the laser damage resistance of fused silica by wet surface cleaning and optimized HF etch process. *Proc. SPIE* **2013**, *8786*, 87860Q.
34. Gao, X.; Feng, G.; Han, J.; Zhai, L. Investigation of laser-induced damage by various initiators on the subsurface of fused silica. *Opt. Express* **2012**, *20*, 22095–22101. [[CrossRef](#)] [[PubMed](#)]
35. Moncayo, M.A.; Santhanakrishnan, S.; Vora, H.D.; Dahotre, N.B. Computational modeling and experimental based parametric study of multi-track laser processing on alumina. *Opt. Laser Technol.* **2013**, *48*, 570–579. [[CrossRef](#)]

36. Wang, X.; Shen, Z.H.; Lu, J.; Ni, X.W. Laser-induced damage threshold of silicon in millisecond, nanosecond, and picosecond regimes. *J. Appl. Phys.* **2010**, *108*, 033103.
37. Samant, A.N.; Dahotre, N.B. Laser machining of structural ceramics—A review. *J. Eur. Ceram. Soc.* **2009**, *29*, 969–993. [[CrossRef](#)]
38. Timoshenko, S.P.; Goodier, J.N. *Theory of Elasticity*, 3rd ed.; McGraw-Hill Book Company: New York, NY, USA, 1970; pp. 1248–1297. 1297.
39. Lide, D.R. *Handbook of Chemistry and Physics*, 84th ed.; CRC Press: Boca Raton, FL, USA, 2003; pp. 27–80.
40. Martienssen, W.; Warlimont, H. *Handbook of Condensed Matter and Materials Data*, 1st ed.; Springer: New York, NY, USA, 2005; pp. 161–407, 523–559.
41. Walker, P.; Tarn, W.H. *Handbook of Metal Etchants*, 1st ed.; CRC Press: Boca Raton, FL, USA, 1991; pp. 76–106, 719–738.
42. Sato, K.; Yugami, H.; Hashida, T. Effect of rare-earth oxides on fracture properties of ceria ceramics. *J. Mater. Sci.* **2004**, *39*, 5765–5770. [[CrossRef](#)]
43. Miller, P.E.; Suratwala, T.I.; Wong, L.L.; Feit, M.D.; Menapace, J.A.; Davisand, P.J.; Steele, R.A. The Distribution of Subsurface Damage in Fused Silica. *Proc. SPIE* **2005**, *5991*, 599101.
44. Cheng, J.; Chen, M.; Liao, W.; Wang, H.; Xiao, Y.; Li, M. Fabrication of spherical mitigation pit on KH_2PO_4 crystal by micro-milling and modeling of its induced light intensification. *Opt. Express* **2013**, *21*, 16799–16813. [[CrossRef](#)] [[PubMed](#)]
45. Hu, G.; Zhao, Y.; Li, D.; Xiao, Q.; Shao, J.; Fan, Z. Studies of laser damage morphology reveal subsurface feature in fused silica. *Surf. Interface Anal.* **2010**, *42*, 1465–1468. [[CrossRef](#)]



© 2017 by the authors. Licensee MDPI, Basel, Switzerland. This article is an open access article distributed under the terms and conditions of the Creative Commons Attribution (CC BY) license (<http://creativecommons.org/licenses/by/4.0/>).